Volume 13
Number 25
7 July 2022
Pages 7367–7658

Chemical Science

rsc.li/chemical-science

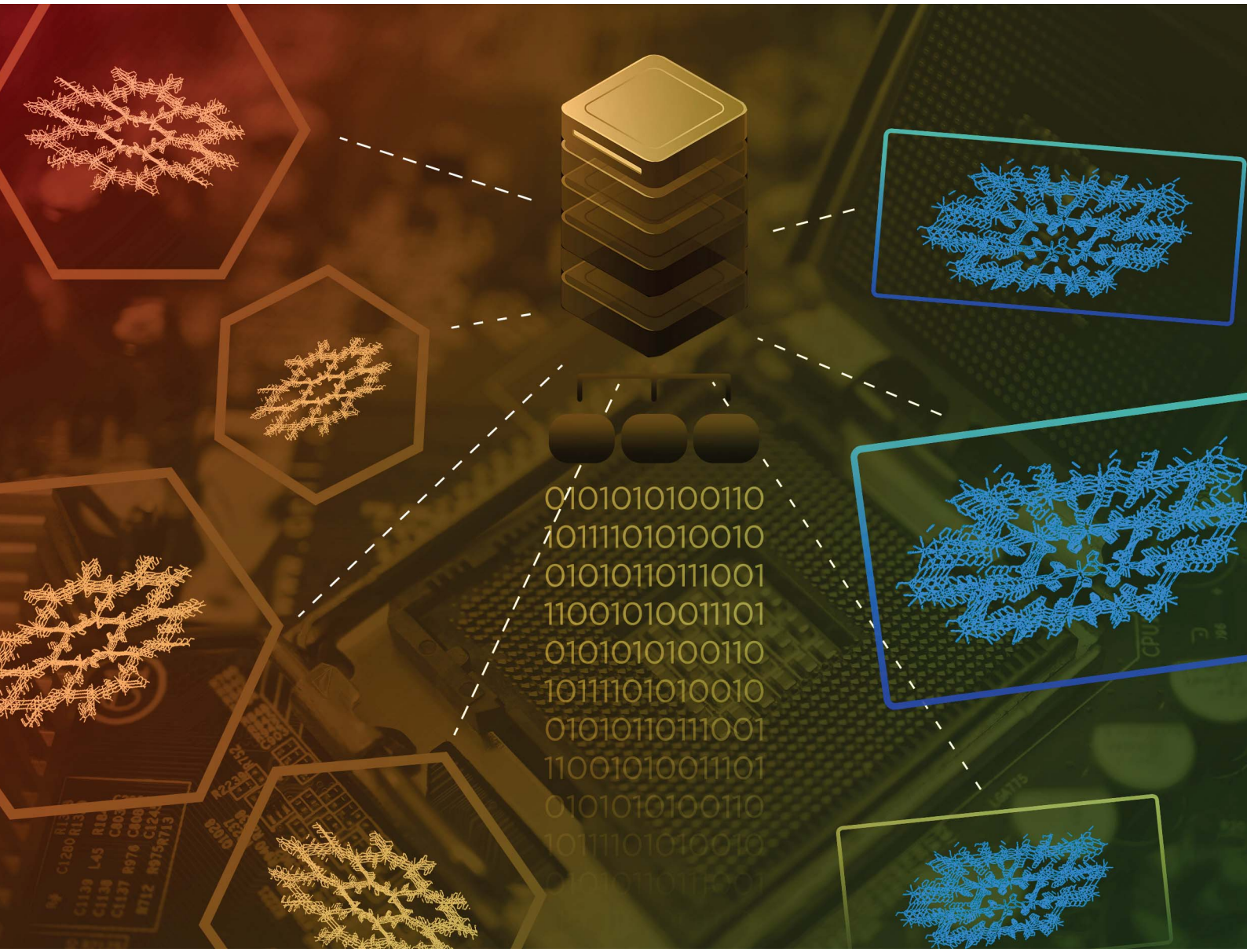

ISSN 2041-6539

ROYAL SOCIETY OF CHEMISTRY

EDGE ARTICLE

Francesco Quochi, Miguel Clemente-León, Maria Laura Mercuri, Eugenio Coronado *et al.*
Reversible Tuning of Luminescence and Magnetism in a Structurally Flexible Erbium-Anilato MOF

Chemical Science

ROYAL SOCIETY OF CHEMISTRY

EDGE ARTICLE

View Article Online
View Journal | View Issue

Cite this: *Chem. Sci.*, 2022, **13**, 7419

All publication charges for this article have been paid for by the Royal Society of Chemistry

Reversible tuning of luminescence and magnetism in a structurally flexible erbium–anilato MOF†

Noemi Monni,[abd] José J. Baldoví,[b] Víctor García-López,[b] Mariangela Oggianu,[ad] Enzo Cadoni,[a] Francesco Quochi,*[cd] Miguel Clemente-León,*[b] Maria Laura Mercuri*[ad] and Eugenio Coronado[b]

By combining 3,6-*N*-ditriazolyl-2,5-dihydroxy-1,4-benzoquinone (H_2trz_2An) with NIR-emitting Er^{III} ions, two different 3D neutral polymorphic frameworks (**1a** and **1b**), differing in the number of uncoordinated water molecules, formulated as $[Er_2(trz_2An)_3(H_2O)_4]_n \cdot xH_2O$ ($x = 10$, **a**; $x = 7$, **b**), have been obtained. The structure of **1a** shows layers with (6,3) topology forming six-membered rings with distorted hexagonal cavities along the *bc* plane. These 2D layers are interconnected through the N4 atoms of the two pendant arms of the trz_2An linkers, leading to a 3D framework, where neighboring layers are eclipsed along the *a* axis, with hexagonal channels filled with water molecules. In **1b**, layers with (6,3) topology in the [101] plane are present, each Er^{III} ion being connected to three other Er^{III} ions through bis-bidentate trz_2An linkers, forming rectangular six-membered cavities. **1a** and **1b** are multifunctional materials showing coexistence of NIR emission and field-induced slow relaxation of the magnetization. Remarkably, **1a** is a flexible MOF, showing a reversible structural phase transition involving shrinkage/expansion from a distorted hexagonal 2D framework to a distorted 3,6-brickwall rectangular 3D structure in $[Er_2(trz_2An)_3(H_2O)_2]_n \cdot 2H_2O$ (**1a_des**). This transition is triggered by a dehydration/hydration process under mild conditions (vacuum/heating to 360 K). The partially dehydrated compound shows a sizeable change in the emission properties and an improvement of the magnetic blocking temperature with respect to the hydrated compound, mainly related to the loss of one water coordination molecule. Theoretical calculations support the experimental findings, indicating that the slight improvement observed in the magnetic properties has its origin in the change of the ligand field around the Er^{III} ion due to the loss of a water molecule.

Received 7th February 2022
Accepted 10th May 2022

DOI: 10.1039/d2sc00769j

rsc.li/chemical-science

Introduction

Metal–organic frameworks (MOFs), formed by organic molecules (linkers) and metal ions (nodes), are attracting considerable attention in materials science thanks to their fascinating architectures[1,2] and the richness of their chemical and physical properties. Noteworthily, some of them possess structural flexibility,[3] a unique feature that depends on the nature of metal–ligand interactions, which in turn, is influenced by both organic ligands and metal ions/clusters. As a direct consequence, flexible MOFs show dynamic properties such as opening/closing of pores, expansion/shrinkage of the framework and/or a reversible change of physical properties, induced by different types of stimuli such as light, electrical potential, pressure or inclusion of guest molecules.[4–6] Despite the plethora of MOFs reported so far, those showing structural flexibility and dynamic behaviour are rare, in spite of their great potential in several applications, including storage, sensing and biomedicine. More importantly, this uncommon feature makes MOFs a challenging platform for designing multiple functionalities with the possibility to tune the physical properties upon reversible structural changes in response to external stimuli.[7,8] Lanthanide based MOFs (Ln^{III}-MOFs) in particular show peculiar luminescence properties with emission in the Vis to NIR range.[9] In fact, Ln^{III}-MOFs can enable strong light absorption by the organic linkers and efficient lanthanide emission sensitization *via* the so-called antenna effect, thereby circumventing the inherently low optical absorption rates due to the Ln^{III} forbidden f–f transitions. In addition, Ln^{III} ions possess large inherent magnetic anisotropy, *i.e.* large unquenched orbital angular moments,

[a]*Dipartimento di Scienze Chimiche e Geologiche, Università degli Studi di Cagliari, Complesso Universitario di Monserrato, 09042 Monserrato, Italy. E-mail: mercuri@unica.it*

[b]*Instituto de Ciencia Molecular, Universitat de València, Catedrático José Beltrán 2, 46980 Paterna, Spain. E-mail: miguel.clemente@uv.es*

[c]*Dipartimento di Fisica, Università degli Studi di Cagliari, Complesso Universitario di Monserrato, 09042 Monserrato, Italy. E-mail: quochi@unica.it*

[d]*Consorzio Interuniversitario Nazionale per la Scienza e Tecnologia dei Materiali, INSTM, Via Giusti 9, 50121 Firenze, Italy*

† Electronic supplementary information (ESI) available. CCDC 2130639–2130642. For ESI and crystallographic data in CIF or other electronic format see https://doi.org/10.1039/d2sc00769j

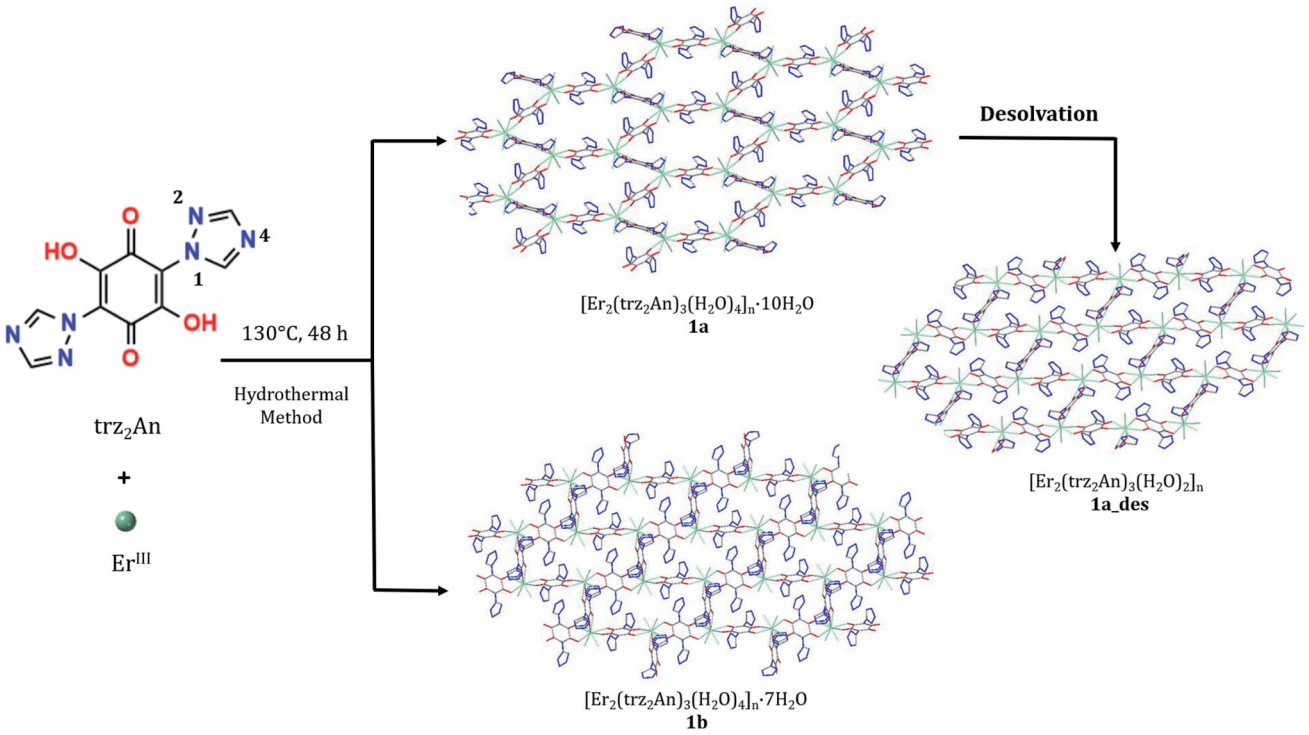

Scheme 1 Synthetic strategy for **1a**, **1a_des** and **1b**.

which impart strong magnetic anisotropy. Their interesting magnetic behaviour makes them attractive candidates to build single-ion magnets (SIMs),[10] a class of mononuclear metal complexes exhibiting slow magnetic relaxation of molecular origin. Controlled spatial organization of SIMs to build large-scale ordered arrays can be achieved by assembling Ln^{III} ions into a 3D framework affording the so-called SIM-MOF.[11,12] Among the organic linkers which can either act as a powerful antenna or isolate magnetically the Ln^{III} metal ions, 3,6-disubstituted (X)-2,5-dihydroxybenzoquinone derivatives with X = H, F, Cl, Br, I or CN (*i.e.* anilates) have recently been studied as building blocks for Ln^{III}-based frameworks,[13–16] leading to several bi-dimensional (2D) and a few three-dimensional (3D) lattices[17–20] with interesting properties such as luminescence, SIM behaviour, gas/solvent adsorption/desorption and solvent exchange.[21] These bridging ligands couple (antiferro)magnetically the transition metal centers but they provide a good magnetic isolation with Ln^{III} metal ions as a result of the negligible overlap with the 4f orbitals.[21] Additionally, redox-activity of the benzoquinone core has been shown to be a challenging strategy to tune (enhancing) magnetism and conductivity in benzoquinone-based 3D/2D frameworks and related nanostructures.[22,23] Interestingly, Pontilliart *et al.* reported the first simultaneous reversible redox- and solvato-magnetic switching, observed in a dinuclear Dy^{III} single-molecule magnet (SMM) complex based on a tetrathiafulvalene triad, through a reversible dehydration/rehydration process of the Dy^{III} coordination sphere. Redox-activity plays a crucial role in the modulation of the Dy^{III} magnetic relaxion through the addition of one water molecule. A significant modulation of SMM behaviour due to a hydration/dehydration process has been also observed in the $Na_9[Er(W_5O_{18})_2]\cdot 35H_2O$ polyoxometalate.[24,25] Previous attempts to tune the magnetic and optical properties of Ln^{III}-anilato-based frameworks, based on the exchange of coordinated and non-coordinated solvent molecules, were reported as well, even though not accompanied by drastic structural changes.[16] In the present work, the 3,6-*N*-ditriazolyl-2,5-dihydroxy-1,4-benzoquinone (H_2trz_2An) anilato derivative (Scheme 1)[26] has been used to construct 3D MOFs, thanks to the coordinative properties of the N4 atoms of the two triazole pendant arms at the 3,6 positions of the anilato moiety. Indeed, it has afforded a Mn^{II} 3D coordination polymer[27] and ultramicroporous Co^{II} 3D MOFs, featuring an excellent capability in CO_2 capture and separation.[28] By resorting to Ln^{III} ions – in particular, the NIR emitting luminescent Er^{III} ion – two 3D Er^{III}-based frameworks formulated as $[Er_2(trz_2An)_3(H_2O)_4]_n\cdot 10H_2O$ (**1a**, porous) and $[Er_2(trz_2An)_3(H_2O)_4]_n\cdot 7H_2O$ (**1b**, non-porous), have been obtained. These polymorphs were characterized by single-crystal X-ray diffraction (SC-XRD), luminescence spectroscopy and magnetometry, showing that both compounds present a field-induced slow relaxation of magnetization. Interestingly, all techniques proved a reversible structural flexibility and shrinkage/expansion dynamic behaviour of the **1a** framework that originate from a change in the coordination environment of Er^{III} ions, in response to the removal of coordinative water molecules. Noteworthily, such a structural flexibility induces important and reversible structural changes after partial dehydration, thus allowing for a tuning of their SIM

and luminescence properties, which can be rationalized by means of effective electrostatic ligand field calculations.

Results and discussion

Synthesis

By combining $Er(NO_3)_3 \cdot 6H_2O$ with H_2trz_2An in a 1 : 1 ratio, $[Er_2(trz_2An)_3(H_2O)_4]_n \cdot 10H_2O$ (**1a**) and $[Er_2(trz_2An)_3(H_2O)_4]_n \cdot 7H_2O$ (**1b**) were obtained through a hydrothermal method (Scheme 1). Isostructural compounds are also obtained with Tb^{III}, Dy^{III} and Ho^{III} which will be published in due course. The synthetic protocol has been optimized for the Er^{III} derivative because it presents multifunctionality. Two types of crystals were observed in each hydrothermal batch: dark red block crystals (**1a**) and orange prismatic crystals (**1b**) (Fig. S1a†). Due to the difference in density, it was possible to separate both types of crystals by using a CH_2Cl_2/CH_2Br_2 solvent mixture. Thus, when the crystals were suspended in the CH_2Cl_2/CH_2Br_2 solution, crystals of **1a** started floating, while crystals of **1b** lied at the bottom (Fig. S1b†). The lower density of **1a** agrees with the more porous structure of this compound, which is formed by interconnected hexagonal pores, in contrast to **1b** with rectangular pores of smaller size (*vide infra*). In an attempt to decrease the number of solvate water molecules of **1a** in a controlled way, by heating or applying vacuum, a drastic and reversible structural change was observed. By contrast, the **1b** structure remains unaltered under the same aforementioned conditions. The removal of some of water molecules present in the channels and one coordinated water molecule in **1a** results in a new crystalline phase, $[Er_2(trz_2An)_3(H_2O)_2]_n \cdot 2H_2O$ (**1a_des**), with a less porous structure formed by distorted rectangular cavities (*vide infra*).

Crystal structure

The structures of **1a** and **1b** were obtained at 120 K by SC-XRD. Both compounds crystallize in the triclinic space group $P\bar{1}$. They are 3D neutral coordination frameworks formed by Er^{III} ions connected by trz_2An bridging linkers. In **1a**, the Er^{III} ion is ennea-coordinated with a $\{NO_8\}$ coordination sphere arising from two oxygens of three bidentate trz_2An anilates, the N4 atom of one trz_2An and two coordinated water molecules. The geometry of the first coordination sphere is closest to a spherical capped square antiprism (CSAPR-9) according to continuous SHAPE analysis (Fig. 1a and Table S9†).[29] Er^{III} ions are linked to three neighboring ions through the oxygens of three trz_2An anilates which coordinate in the bis-bidentate mode. This leads to layers with (6,3) topology forming six-membered rings with distorted hexagonal cavities along the *bc* plane (Fig. S2a†). Each cavity contains two anilato rings almost parallel to the layer (face-on) and four anilato rings almost perpendicular to it (edge-on). The largest Er–Er–Er angle in the hexagon is 134.4°, while the Er–Er distances of the diagonals of the hexagons are 12.8, 13.4 and 21.9 Å (Table S4†). These distances and angles are similar to those found in Ln^{III}–anilato-based 2D compounds with an ennea-coordinated ligand field for the Ln^{III} and spherical tricapped trigonal prism (TCTPR-9) geometry.[30,31] The C–O and C–C bond lengths across the five-membered chelate ring for trz_2An ligands also present typical values of anilato dianions (see Table S3†).[30] A remarkable difference with respect to previous Ln^{III} anilato-based 2D compounds is that these 2D layers are interconnected through the N4 atoms of the two 1,2,4-triazole substituted pendant arms of one of the three trz_2An linkers coordinated to each Er^{III} (face-on linkers) (Fig. 1c). This leads to a porous 3D framework, where neighboring layers are eclipsed along the *a* axis with hexagonal channels filled with water molecules (Fig. 1b). The remaining

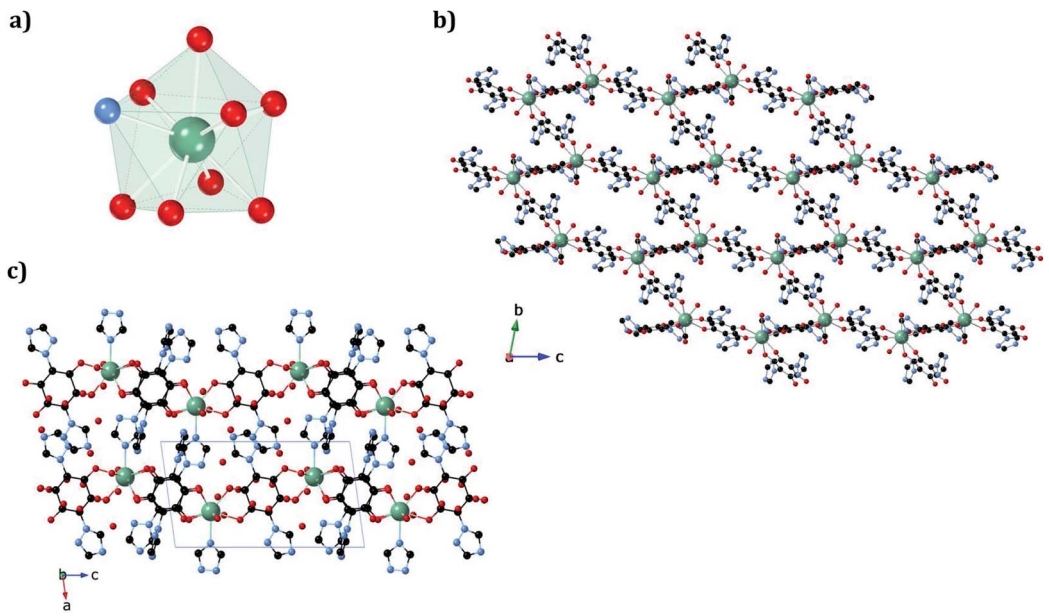

Fig. 1 (a) Spherical capped square antiprismatic coordination geometry of the Er^{III} center in **1a**. (b) View of **1a** along the *bc* plane, showing hexagonal cavities. (c) View of **1a** along the *ac* plane, showing layers bridged by trz_2An linkers. The black, blue, red, and green spheres represent the C, N, O, and Er^{III} atoms, respectively. Hydrogen atoms and water molecules inside the pores are omitted for clarity.

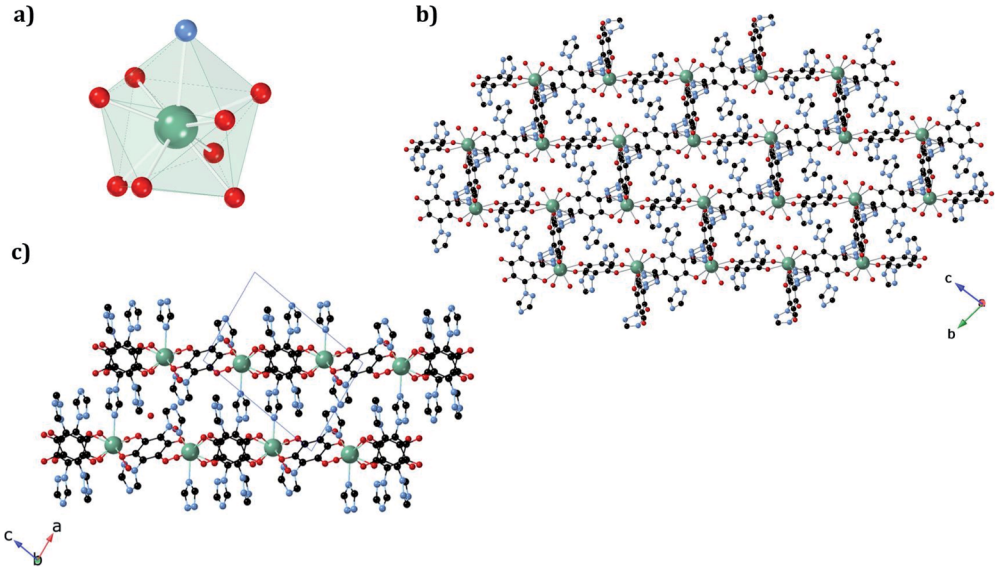

Fig. 2 (a) Spherical tricapped trigonal prismatic coordination geometry of the Er^{III} center in **1b**. (b) View along the *bc* plane, showing rectangular cavities. (c) View along the *ac* plane of **1b**, showing layers bridged by trz_2An linkers. The black, blue, red, and green spheres represent the C, N, O, and Er^{III} atoms, respectively. Hydrogen atoms and water molecules inside the pores are omitted for clarity.

N4 atoms of the 1,2,4-triazole substituted pendant arms of the other two trz_2An linkers are hydrogen-bonded to coordinating water molecules.

In **1b**, the Er^{III} ion is ennea-coordinated as well, showing a $\{NO_8\}$ coordination sphere with six oxygens of three bidentate trz_2An linkers, two coordinated water molecules and the N4 atom of one trz_2An ligand. The coordination geometry is nearest to a spherical tricapped trigonal prism (TCTPR-9) according to continuous SHAPE analysis[29] (Fig. 2a and Table S9†). The structure shows layers with (6,3) topology in the [101] plane, in which each Er^{III} ion is connected to three other Er^{III} ions through bis-bidentate trz_2An linkers forming rectangular six-membered cavities, which adopt a brick-wall structure where the long axes of all the rectangles are parallel (Fig. S2b†). Thus, the two largest Er–Er–Er angles are close to 180° (172.5°) (see Table S6†). On the other hand, Er^{III} nodes of the same layer are almost coplanar and are connected to Er^{III} nodes of other layers, through the N4 atom of the two pending triazolyl arms of one of the three trz_2An linkers (Fig. 2c), which are placed at the shortest side of the rectangular cavities, leading to a 3D framework. Finally, the C–O and C–C bond lengths across the five-membered anilato ring for trz_2An linkers exhibit, as in **1a**, typical values of anilato dianions (see Table S5†).[30] The powder X-ray diffraction (PXRD) patterns of both **1a** and **1b** polycrystalline samples are fully consistent with the calculated ones (Fig. S3 and S4†), confirming the homogeneity and purity of the bulk sample. These polycrystalline samples were placed under vacuum in a Schlenk line and then sealed in a glove box in order to study if the vacuum could induce changes in the crystal structure. A structural change was observed in **1a** leading to a new phase, **1a_des**, where a loss of water molecules was found. Instead, no structural change was observed for **1b**, as clearly shown in Fig. S5.† Remarkably, when **1a_des** was left in air for two days, the sample is rehydrated forming the **1a** phase as shown by PXRD measurements (Fig. 3). This proves that the dehydration/hydration process and the induced structural change are fully reversible.

The structure of the new dehydrated phase, **1a_des**, was investigated by SC-XRD. A vacuum was applied to a single crystal of **1a**, which was then transferred to a diffractometer at 120 K. A similar structure was obtained if a single crystal of **1a** was heated at 360 K in the diffractometer with a small difference in the water pore content. The Er^{III} ion in **1a_des** (under vacuum/heating) shows a $\{NO_7\}$ coordination sphere arising from six oxygens of three bidentate trz_2An linkers, the N4 atom of one trz_2An linker and one coordinated water molecule, different from the $\{NO_8\}$ one observed in **1a**. This is due to the loss of one water coordination molecule. The coordination geometry is close to a triangular dodecahedron (TDD-8) (Fig. 4a

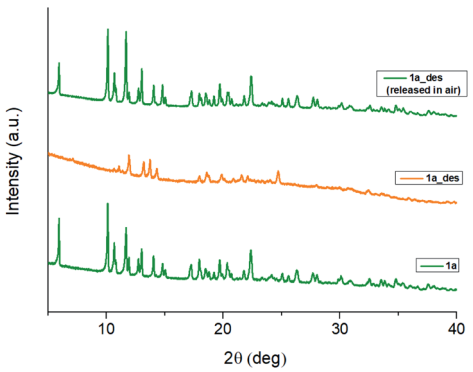

Fig. 3 PXRD patterns of **1a** (green), **1a_des** (orange) and **1a_des** left in air 2 days after vacuum treatment (green top), highlighting the full reversibility of the structural change induced by dehydration.

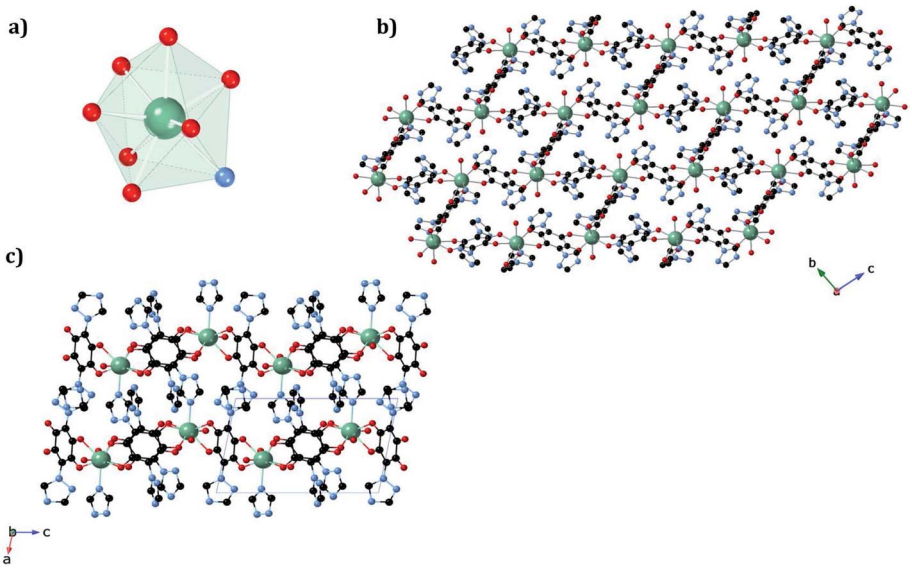

Fig. 4 (a) Triangular dodecahedron coordination geometry of the Er^{III} ions in **1a_des**. (b) View along the *bc* plane of the **1a_des** framework, showing shrunk rectangular cavities. (c) View along the *ac* plane of **1a_des**, showing layers bridged by trz_2An linkers. The black, blue, red, and green spheres represent the C, N, O, and Er^{III} atoms, respectively. Hydrogen atoms and water molecules inside the pores are omitted for clarity.

and Table S10†), according to continuous SHAPE analysis.[29] Er–O bond lengths are in the range of 2.266(16)–2.430(16) Å for **1a_des** after vacuum (2.28(2)–2.442(13) Å for **1a_des** at 360 K), while Er–N bond lengths are 2.46(2) Å for **1a_des** after vacuum (2.464(18) Å for **1a_des** at 360 K). Again, the C–O and C–C bond lengths across the five-membered anilato ring for trz_2An linkers exhibit typical values of anilato dianions,[30] 1.22(3)–1.26(2) and 1.57(3)–1.60(3) Å for **1a_des** after vacuum (1.22(3)–1.27(2) and 1.52(3)–1.54(3) Å for **1a_des** at 360 K) (see Table S7†). As in the **1a** case, the structure shows layers with (6,3) topology in the *bc* plane, but interestingly, they exhibit a drastic change from a distorted hexagonal 2D network to a distorted 3,6-brickwall rectangular structure. Thus, the six-membered rectangular cavities of the layers contain four face-on and two edge-on anilato rings in **1a_des**, instead of the two face-on and four edge-on ones found in **1a** (Fig. S2b†). Remarkably, the 3D framework is maintained thanks to the N4 atom of the two pending triazolyl arms of one of the three trz_2An linkers located in the shortest side of the rectangular cavity (face-on linker), indicating that the connectivity is the same as that of **1a**. Neighboring layers are eclipsed along the *a* axis, leading to rectangular channels (Fig. 4b). These channels contain one crystallographically independent water solvate molecule forming a hydrogen bond with the coordinated water molecule. By heating the sample at 360 K, the solvate water molecule shows a disorder, and it was modeled with an occupancy of 0.5. This could be related to a more complete dehydration of the sample. As shown by PXRD, the phase of **1a_des** is consistent with the calculated one from the CIF (Fig. S6†).

In conclusion, a structural phase transition from a hexagonal cavity to a rectangular one is observed when the **1a** phase is dehydrated under vacuum or by heating the sample. This transition is fully reversible, as observed when the dehydrated phase (**1a_des**) is rehydrated.

Magnetic properties

DC magnetic susceptibility measurements of **1a**, **1b**, and **1a_des** were carried out in the temperature range of 2–300 K using an applied magnetic field of 0.1 T (Fig. 5 and S10†). In the case of **1a**, it was necessary to perform the measurements in a closed holder and in contact with H_2O to prevent its dehydration and subsequent formation of **1a_des** due to the vacuum of the squid chamber (~2–3 mbar). We measure a $\chi_M T$ product at 300 K of 11.43 (**1a**), 11.36 (**1b**) and 11.58 (**1a_des**) $cm^3\ K\ mol^{-1}$, which is close to the value expected for Er^{III} (11.475 $cm^3\ K\ mol^{-1}$; $^4I_{15/2}$), thus indicating that most of the ligand field split energy levels of the ground multiplet are populated at room temperature. $\chi_M T$ shows a slow and steady decrease upon cooling from 300 K to 50 K, which becomes sharper at lower temperatures reaching a value of 5.2, 5.5 and 6.1 $cm^{-3}\ K\ mol^{-1}$ for **1a**, **1b** and **1a_des**, respectively at 2 K. The decrease at low temperature is characteristic of the depopulation of these levels. The field dependence of magnetization was also measured in the 2–8 K temperature range by varying the magnetic field up to 5 T (Fig. S11 and S12†).

To further understand the observed magnetic behaviour of both phases, theoretical calculations were carried out using the SIMPRE computational package.[32] The static magnetic susceptibility was successfully fitted by using the radial effective charge (REC) model[33] ($D_r = 0.98$ Å and $Z_i = 0.161$ for oxygens, and $D_r = 1.20$ Å and $Z_i = 0.05$ for nitrogen) (Fig. 5 and S10†). This allowed the prediction of the magnetization curves, which are also in good agreement with the experimental data (Fig. S11 and S12†). The diagonalization of the crystal field Hamiltonian results in a ground state wave function mainly composed of

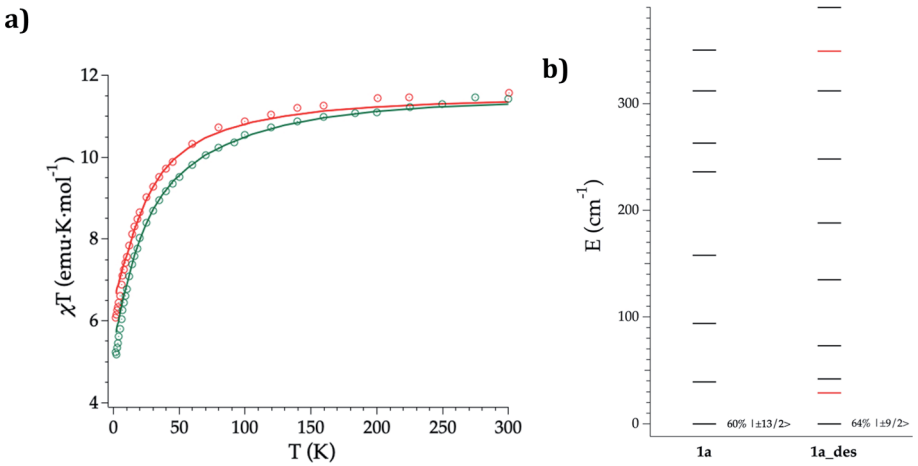

Fig. 5 Experimental (symbols), fitted (solid line) temperature-dependence of the magnetic susceptibility from 2 to 300 K of **1a** (green) and **1a_des** (red) (a); calculated (black) and experimental (red) ground-*J* multiplet energy levels (b). Further details are provided in Table S13.†

60% of the $M_J = |\pm 13/2\rangle$ microstate in the easy axis direction for **1a** and **1b**, which is congruent with the observed slow relaxation of the magnetization. The first excited doublet is located at about 39 cm^{-1} and is mainly composed of the $M_J = |\pm 11/2\rangle$ microstate (37%), mixed with $|\pm 3/2\rangle$ and $|\pm 1/2\rangle$ for **1a**, while it is located at about 32 cm^{-1} and is mainly composed of $|\pm 15/2\rangle$ and $|\pm 11/2\rangle$ (63% between both of them) for **1b**. The energy levels are approximately equispaced, and the total crystal field splitting reaches 355 cm^{-1}. In the case of **1a_des**, the loss of a water molecule that reduces the coordination number results in a drastic change of the ground state wave function, which is now described by a mixture between $|\pm 9/2\rangle$ (64%), $|\pm 11/2\rangle$ (14%) and $|\pm 7/2\rangle$ (11%) microstates, while the first excited energy level is located at 42 cm^{-1} (see Tables S13 and S14†).

The dynamic magnetic properties were studied by susceptibility measurements performed with an alternating magnetic field (AC susceptibility). In the absence of a magnetic field, no signal in the out-of-phase molar susceptibility (χ'') was observed. When magnetic DC fields of 0.09 T were applied, strong frequency-dependent peaks in both the in-phase molar susceptibility (χ') and χ'' appear with clear maxima of χ'' below 2.2 K for **1a** (Fig. S13†). On the other hand, the variable-frequency AC data of **1a** at 2 K show a maximum at *ca.* 5800 Hz in χ'' (see Fig. 6). This is a clear indication that **1a**

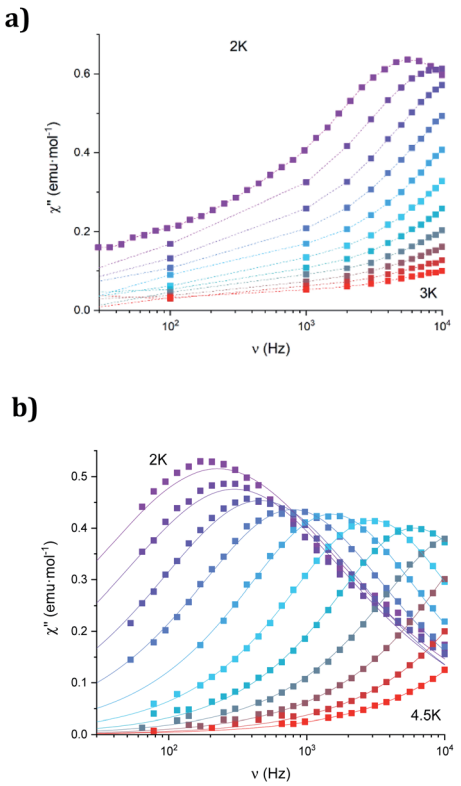

Fig. 6 Frequency dependence of the out-of-phase component, χ'', of **1a** (a) and **1a_des** (b) in an applied DC field of 0.09 T at the different temperatures. Solid lines represent the best fits to the Debye model.

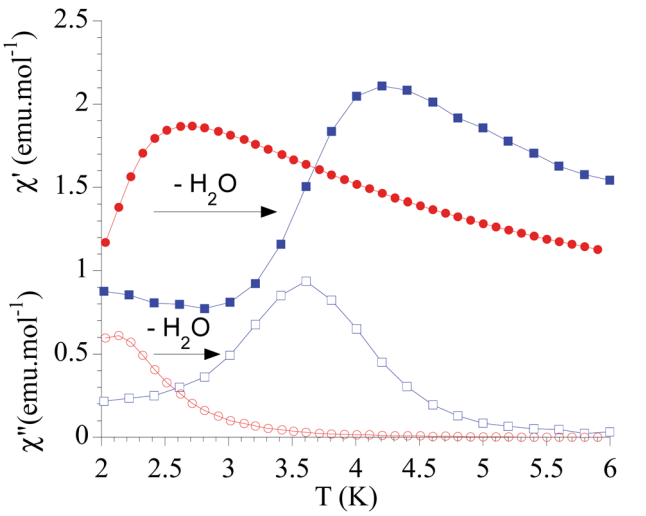

Fig. 7 Temperature dependence of χ' and χ'' of **1a** (full and empty red circles, respectively) and **1a_des** (full and empty blue squares, respectively) in an applied DC field of 0.09 T at 10 000 Hz.

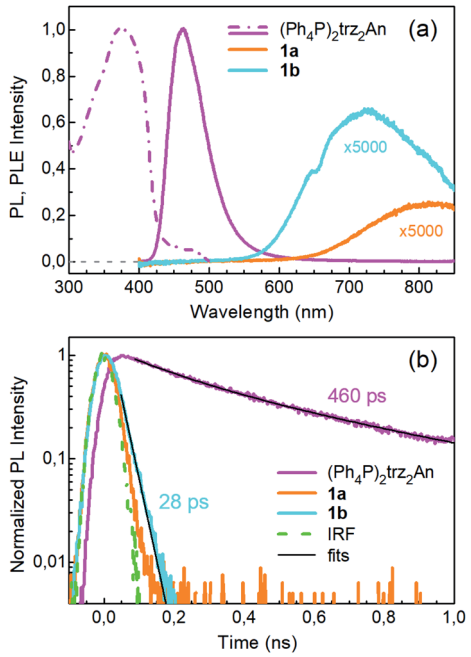

Fig. 8 Ligand-centred PL properties of **1a**, **1b** and the reference $(Ph_4P)_2(trz_2An)$ linker, under 355 nm pulsed laser irradiance. (a) Ligand-centred PL spectra acquired under standard conditions and normalized to the peak of the spectrum of $(Ph_4P)_2trz_2An$. The PL intensities of **1a** and **1b** are multiplied by a factor of 5000. The dashed-dotted line is the normalized PL excitation (PLE) spectrum of $(Ph_4P)_2trz_2An$. The excitation spectra of the strongly quenched ligand emissions of **1a** and **1b** could not be clearly detected and are not shown. (b) Spectrally-integrated ligand-centred PL decay transients and the impulse response function (IRF) of the detection setup. The fit of a three exponential decay curve to the $(Ph_4P)_2trz_2An$ decay is shown, and the amplitude-averaged lifetime is indicated. Monoexponential fit of the **1b** decay and the lifetime are reported as well.

presents a field-induced slow relaxation of magnetization. Interestingly, when **1a** is dehydrated to give **1a_des**, the χ'' maxima are shifted to higher temperatures (3.6 K for **1a_des** and 2.2 K for **1a** at a frequency of 10 000 Hz under an applied DC field of 0.09 T) and at lower frequencies in the variable-frequency AC measurements (5800 Hz for **1a** and 170 Hz for **1a_des** at 2 K) as shown in Fig. 6 and 7. When the same desolvated sample is measured again in contact with H_2O, the initial magnetic behavior of **1a** is restored in a reversible way. This result confirms that the structural changes of **1a** after dehydration modify the magnetic properties, in agreement with the decrease of the mixing with lower microstates found from the theoretical calculations for **1a_des**. Thus, although the ground state of **1a_des** is dominated by a lower M_J value than for **1a**, importantly, most of the wave function is described by high M_J values (88% between $|\pm 11/2\rangle$, $|\pm 9/2\rangle$ and $|\pm 7/2\rangle$), thus resulting in a more negligible contribution from those with lower M_J values. This situation is more favourable to reduce fast spin relaxation through quantum tunneling of the magnetization (QTM) at low temperatures in **1a_des**. In contrast, in **1a**, the non-negligible contribution of nonaxial crystal-field terms increases the coupling to the degenerate Kramers doublets in high-order perturbation theory[34] leading to poorer SMM properties. Another interesting aspect is that the loss of a water molecule erases its molecular vibrations, preventing them from coupling with the ligand field split energy levels, thus suppressing this possible vibration-induced magnetic relaxation channel.[35] It is likely that the combination of both effects (a reduction in QTM and molecular vibrations) is responsible for the slight increase in the blocking temperature of **1a** after dehydration, as dynamic magnetic measurements indicate. Interestingly, the modulation of SIM properties has not been observed in the isostructural Dy-MOF.[36]

The Cole–Cole plots (χ'' *vs.* χ') of **1a_des** confirm the presence of a single relaxation process (see Fig. S15†). Thus, at fixed temperatures between 2.0 and 3.5 K, semi-circular plots were obtained and fitted using a generalized Debye model, yielding the α parameter in the range of 0.17–0.40. This indicates moderately broad distributions of the relaxation processes. In the case of **1a**, only one temperature could be studied due to the lower temperature of the maxima in χ'' (see Fig. S15†). Again, the Cole–Cole plot at this temperature suggests the presence of a single relaxation process ($\alpha = 0.31$). The relaxation times (τ) of **1a_des** at the different temperatures were determined from the Debye model. They were fitted to the Arrhenius expression for a thermally activated process (Orbach, $\tau = \tau_0 \exp(U_{eff}/k_BT)$). However, the plots of τ *vs.* $1/T$ deviate from linearity at low temperatures, indicating the coexistence of multiple relaxation pathways as observed in other anilate-based Ln^{III} complexes (Fig. S16†). We, therefore, applied the general model where the first, second, third and fourth terms include quantum tunneling, direct, Raman and Orbach relaxation processes, respectively.

$$\tau^{-1} = \tau_{QTM}{}^{-1} + AH^2T + CT^n + \tau_0{}^{-1}\exp(-U_{eff}/K_BT)$$

Accurate fittings were obtained using Raman and Orbach relaxation processes with values comparable to those found in other anilate-based Ln^{III} compounds with $C = 16(7)\ s^{-1}\ K^{-5.3}$, $\tau_0 = 5.0(5) \times 10^{-10}$ s and $U_{eff} = 39(2)$ K for **1a_des** (Fig. S17†).[16,20,37,38] The calculated value of n (5.3(3)) is smaller than the ideal value of 9 found for Raman processes. This suggests that these Raman-like relaxations are attributed to acoustic and optical vibrations.[39] Finally, temperature dependence of the τ values of **1a** was not fitted because of the lack of data points.

The AC susceptibility measurements of **1b** show strong frequency-dependent peaks in both χ' and χ'' with the clear maxima of χ'' below 4.2 K when a magnetic DC field of 0.1 T was applied (Fig. S18†). The variable-frequency AC data at different temperatures show the maxima of χ'' at 160 Hz at 2 K and *ca.* 6000 Hz at 4 K (see Fig. S19†). Therefore, they indicate a field-induced slow relaxation of magnetization in agreement with theoretical calculations. The Cole–Cole plots (χ'' *vs.* χ') confirm the presence of a single relaxation process (see Fig. S20†). Thus, at fixed temperatures between 2.0 and 4.0 K, semi-circular plots were obtained and fitted using a generalized Debye model, yielding the α parameter in the range of 0.12–0.21. This indicates narrower distributions of the relaxation processes than in

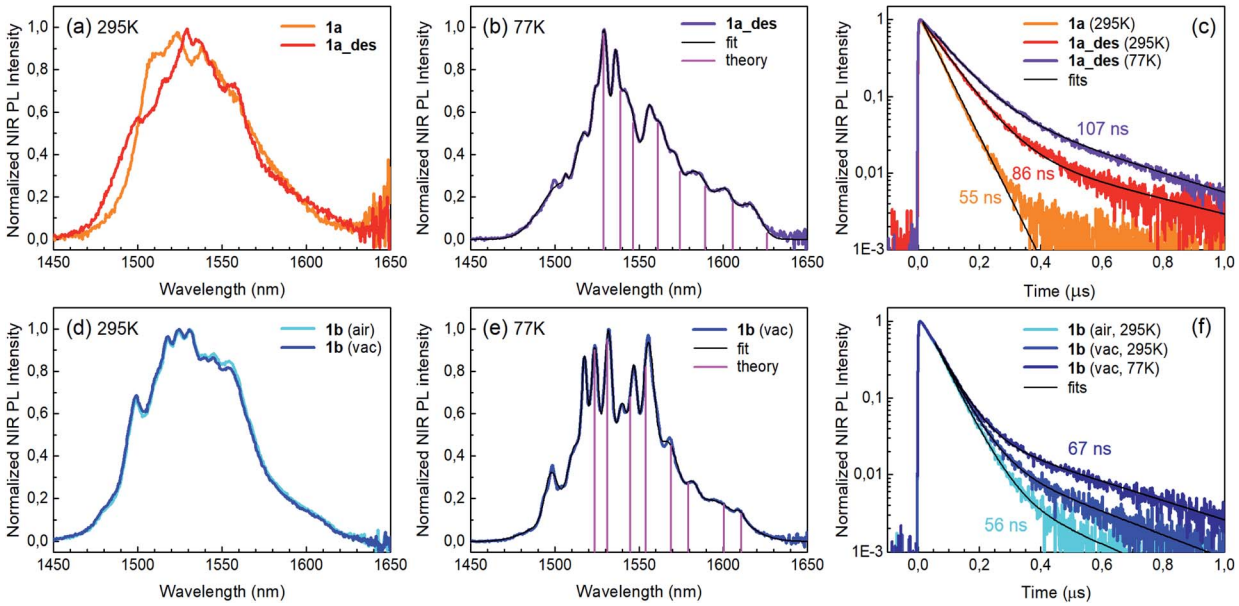

Fig. 9 Er^{III}-centred NIR PL properties of **1a**, **1a_des** and **1b**. (a) PL spectra of **1a** and **1a_des** at room temperature. (b) Low-temperature (77 K) spectrum of **1a_des** with multiple Gaussian fit. Vertical bars represent the radiative transitions from the $^4I_{13/2}$ lowest level to the ground ($^4I_{15/2}$) multiplet levels estimated from theoretical calculations. (c) PL decay transients for **1a** and **1a_des** at room temperature and at 77 K. Biexponential decay fits and amplitude-averaged lifetimes are shown as well. (d)–(f) Same as (a)–(c) but for **1b**.

the case of **1a_des**. Temperature dependence of the τ values of **1b** was fitted using Raman and Orbach relaxation processes with values comparable to those found in **1a_des** and other anilate-based Ln^{III} compounds with $C = 11(5)\ s^{-1}\ K^{-5.6}$, $n = 5.6(4)$, $\tau_0 = 2.0(5) \times 10^{-9}$ s and $U_{eff} = 42(3)$ K (Fig. S17†).[16,20,35,36]

Photoluminescence properties

Photoluminescence (PL) was excited using short laser pulses at a wavelength of 355 nm and analysed both spectrally and temporally. Near UV laser irradiation photoexcites the trz_2An linker dianion in all compounds. Er^{III} emission sensitization then occurs *via* the optical antenna effect through a ligand-to-metal energy relaxation pathway. As clearly seen in Fig. 8a, ligand-centred emission of **1a** and **1b** measured under standard conditions appeared considerably redshifted and quenched with respect to that of the ligand dianion trz_2An in the $(Ph_4P)_2trz_2An$ reference compound. This was rationalized as the consequence of strong singlet/triplet intersystem mixing (heavy-atom effect), ensuing a ligand-centred excited state that quickly relaxes toward the Ln^{III} ion by ligand-to-metal energy transfer.[40] In fact, as deduced by three exponential fitting of the PL decay profile and amplitude averaging of the time constants, the bare excited-state lifetime of trz_2An measured in $(Ph_4P)_2(trz_2An)$ lies in the time scale of hundreds of picoseconds (~460 ps, Fig. 8b), whereas the ligand-centred emission of **1a** is nearly resolution-limited, hinting towards a quantitative ligand-to-metal energy sensitization with nearly unity efficiency. Similar considerations hold for **1b**, where a monoexponential PL lifetime of ~30 ps was observed. At room temperature (295 K), **1a** and **1a_des** exhibited different Er^{III}-centred ($^4I_{13/2} \rightarrow {}^4I_{15/2}$) emission spectra, readily interpreted as a consequence of the different coordination environment experienced by Er^{III} in the two compounds (Fig. 9a). Cooling **1a_des** under vacuum conditions down to 77 K resulted in higher spectral definition of the crystal-field-split $^4I_{13/2} \rightarrow {}^4I_{15/2}$ optical transitions (Fig. 9b). Up to 13 transitions could be clearly detected and fairly well fitted using a multiple Gaussian fit procedure, thereby demonstrating a non-negligible presence of hot bands (starting from higher energy states of the $^4I_{13/2}$ multiplet) still at 77 K.[41] A direct comparison between the emission spectra at 295 and 77 K allowed for a tentative identification of the zero-phonon transition, which was observed at 1529 nm. In turn, this enabled a direct comparison between the observed transition wavelengths and those inferred from the theoretically calculated energy spectrum of the $^4I_{15/2}$ multiplet. Despite the strong vibrational quenching of the Er^{III} emission from coordinated water molecules, effectively reducing the Er^{III} excited-state lifetime from milliseconds to tens of nanoseconds,[42] **1a** and **1a_des** could be quite clearly distinguished on the basis of the decay profiles of the Er^{III}-centred NIR PL, the amplitude-averaged lifetime (extracted from biexponential fits) being 55 ns in **1a** and 86 ns in **1a_des** (Fig. 9c). This was ascribed to the different quenching produced by two coordinated water molecules in **1a** and only one water molecule in **1a_des**. Upon cooling at 77 K, the PL lifetime of **1a_des** increased to 107 ns possibly due to partial suppression of vibrational quenching. The PL properties of **1a** could not be measured at 77 K because the experimental technique used for cryogenic measurements involves **1a** dehydration and consequent phase transition to **1a_des** prior to cooling. As shown in Fig. 9d, **1b** displayed practically the same room-temperature Er^{III}-centred NIR emission spectrum, both in air and under vacuum, in agreement with the results of PXRD measurements and confirming the existence of only one phase. The decay profile of the

NIR PL showed a much lower sensitivity to environmental conditions, which was in part expected since in **1b** the vacuum does not modify the number of water molecules coordinated to the Er^{III} ions (Fig. 9f). Comparison of the 295 and 77 K emission spectra (Fig. 9e) led to the identification of the emission peak centred at 1524 nm as the most probable zero-phonon transition in **1b**, allowing for comparison of experiment and theory just as for **1a_des**.

Reversible phase transition from **1a** to **1a_des** was confirmed spectroscopically by performing several air/vacuum (rehydration/dehydration) cycles, where highly reproducible emission spectra and decay transients were obtained (see Fig. S21†). Overall, theoretical calculations of the ground ($^4I_{15/2}$) multiplet spectra turned out to be consistent with the low-temperature emission spectra, with regard to both the energy splitting between the first two levels and the whole energy spread within the multiplet. The agreement is quite impressive for **1b**, as clearly seen in Fig. 9e.

Conclusions

The H_2trz_2An anilato derivative, bearing a triazole pendant arm at the 3,6 positions of the anilato moiety, has been used for the first time in combination with Er^{III} nodes to afford **1a** and **1b** 3D frameworks formed by 2D layers with (6,3) topology linked through the anilato ligands. A remarkable difference with respect to previous Ln^{III} anilato-based compounds is that these 2D layers are interconnected through the N4 atoms of the two 1,2,4-triazole substituted pendant arms of trz_2An, leading to formation of 3D frameworks. **1a** and **1b** constitute unique examples of multifunctional frameworks as they display NIR emission and field-induced slow relaxation of the magnetization. To the best of our knowledge, this is the first report of an anilato-based Er^{III}-MOF that shows SIM behaviour. Remarkably, the flexibility and porosity of the **1a** MOF enable drastic structural changes after partial dehydration, under very mild conditions (vacuum or heating to 360 K), to a less porous 3D structure in **1a_des**, different from **1b** (*vide supra*). **1a_des** shows an improvement of the magnetic blocking temperature and a modulation of the PL emission spectrum and lifetime, with respect to the hydrated compound, which are mainly related to the loss of one water coordination molecule. Full reversibility of the observed phase transition from **1a** to **1a_des** was demonstrated through several air/vacuum (rehydration/dehydration) cycles. The milder conditions required to achieve the switching from **1a** to **1a_des** and the fact that it affects both luminescent and SIM properties (multifunctionality) in a 3D extended architecture as the flexible anilato-based Er^{III}-MOF, herein reported, constitutes a significant advance with respect to Ln^{III}-based discrete complexes (*vide supra*) showing an interesting solvato-switching of the SIM properties.[24,25] Interestingly, the structure, as well as the luminescent and magnetic properties of **1a**, are fully regenerated by simply exposing the crystals of **1a_des** to air, which constitutes an additional advantage compared to some of the aforementioned molecular complexes.[25]

Theoretical calculations indicate that the slight improvement of SIM properties is mainly due to the decrease of mixing with lower microstates, which reduces quantum tunneling of magnetization at low temperatures. The present work contributes to the ongoing research on flexible MOFs and sheds light on the important role of luminescence spectroscopy and magnetometry as probes for mechanism investigation of flexible Ln^{III}-MOFs.

Author contributions

MLM and NM designed the MOF. MLM, ECa and MCL supervised the research project, with the contribution of ECo and FQ. NM synthesized and characterized the MOF under the supervision of MLM and MCL (structural and magnetic characterization) and with the help of VGL and MO. JJB performed the theoretical calculations and analyzed the magnetic data. FQ performed luminescent experiments and analyzed the data. MLM, MCL and FQ wrote the manuscript. All authors contributed to the final interpretation of the experimental results and critically revised the manuscript. All authors have read and approved the final version of the manuscript.

Conflicts of interest

There are no conflicts to declare.

Acknowledgements

Fondazione di Sardegna – Convenzione triennale tra la Fondazione di Sardegna e gli Atenei Sardi, Regione Sardegna – L.R. 7/2007 Annualità 2018 – DGR 28/21 del 17.05.2015, through Projects F74I19000940007 and F74I19000920007, are acknowledged for the post-doctoral fellowship of MO. MUR (Ministry of Education, University, Research) and UNICA-UNISS Consortium PhD Course on Chemical Sciences and Technologies is also acknowledged for financing the PhD grant of NM. CESA (Centro d'Eccellenza per la Sostenibilità Ambientale, accordo di programma RAS-UNICA-IGEA-AUSI, project number E58C16000080003) is acknowledged for the PhD grant of MO. The CeSAR (Centro Servizi d'Ateneo per la Ricerca) core facility of the University of Cagliari is acknowledged for the use of the Ultrafast Optical Spectroscopy Laboratory. J. J. B. is thankful for support from the Plan Gen-T of Excellence of the Generalitat Valenciana (CDEIGENT/2019/022). Financial support from the EU (ERC Advanced Grant MOL-2D 788222), the Spanish MCIN (Grants PID2020-117264GB-I00 and PID2020-117152RB-I00 funded by MCIN/AEI/10.13039/501100011033 and Unidad de Excelencia María de Maeztu CEX2019-000919-M) and the Generalitat Valenciana (PROMETEO program) is acknowledged. We all thank A. Soriano-Portillo, J. M. Martínez-Agudo and G. Agustí for PXRD and magnetic measurements.

Notes and references

1 H. C. Zhou, J. R. Long and O. M. Yaghi, *Chem. Rev.*, 2012, **112**, 673–674.
2 H. C. J. Zhou and S. Kitagawa, *Chem. Soc. Rev.*, 2014, **43**, 5415–5418.

3 Z. Chang, D. H. Yang, J. Xu, T. L. Hu and X. H. Bu, *Adv. Mater.*, 2015, **27**, 5432–5441.
4 A. Ghoufi, K. Benhamed, L. Boukli-Hacene and G. Maurin, *ACS Cent. Sci.*, 2017, **3**, 394–398.
5 A. Ghoufi, A. Subercaze, Q. Ma, P. G. Yot, Y. Ke, I. Puente-Orench, T. Devic, V. Guillerm, C. Zhong, C. Serre, G. Férey and G. Maurin, *J. Phys. Chem. C*, 2012, **116**, 13289–13295.
6 J. Y. Kim, L. Zhang, R. Balderas-Xicohténcatl, J. Park, M. Hirscher, H. R. Moon and H. Oh, *J. Am. Chem. Soc.*, 2017, **139**, 17743–17746.
7 F. X. Coudert, *Chem. Mater.*, 2015, **27**, 1905–1916.
8 S. M. Hyun, J. H. Lee, G. Y. Jung, Y. K. Kim, T. K. Kim, S. Jeoung, S. K. Kwak, D. Moon and H. R. Moon, *Inorg. Chem.*, 2016, **55**, 1920–1925.
9 S. V. Eliseeva and J. C. G. Bünzli, *Chem. Soc. Rev.*, 2010, **39**, 189–227.
10 L. Sorace, C. Benelli and D. Gatteschi, *Chem. Soc. Rev.*, 2011, **40**, 3092–3104.
11 L. H. G. Kalinke, D. Cangussu, M. Mon, R. Bruno, E. Tiburcio, F. Lloret, D. Armentano, E. Pardo and J. Ferrando-Soria, *Inorg. Chem.*, 2019, **58**, 14498–14506.
12 J. J. Baldoví, E. Coronado, A. Gaita-Ariño, C. Gamer, M. Giménez-Marqués and G. Mínguez Espallargas, *Chem.–Eur. J.*, 2014, **20**, 10695–10702.
13 S. Ashoka Sahadevan, N. Monni, A. Abhervé, D. Marongiu, V. Sarritzu, N. Sestu, M. Saba, A. Mura, G. Bongiovanni, C. Cannas, F. Quochi, N. Avarvari and M. L. Mercuri, *Chem. Mater.*, 2018, **30**, 6575–6586.
14 S. Ashoka Sahadevan, N. Monni, M. Oggianu, A. Abhervé, D. Marongiu, M. Saba, A. Mura, G. Bongiovanni, V. Mameli, C. Cannas, N. Avarvari, F. Quochi and M. L. Mercuri, *ACS Appl. Nano Mater.*, 2020, **3**, 94–104.
15 S. Benmansour, A. Hernández-Paredes, M. Bayona-Andrés and C. J. Gómez-García, *Molecules*, 2021, **26**, 1–21.
16 S. Benmansour, A. Hernández-Paredes, A. Mondal, G. López Martínez, J. Canet-Ferrer, S. Konar and C. J. Gómez-García, *Chem. Commun.*, 2020, **56**, 9862–9865.
17 K. Nakabayashi and S. Ohkoshi, *Inorg. Chem.*, 2009, **48**, 8647–8649.
18 B. F. Abrahams, J. Coleiro, K. Ha, B. F. Hoskins, S. D. Orchard and R. Robson, *J. Chem. Soc., Dalton Trans.*, 2002, **2**, 1586–1594.
19 K. Bondaruk and C. Hua, *Cryst. Growth Des.*, 2019, **19**, 3338–3347.
20 A. Mondal, S. Roy and S. Konar, *Chem.–Eur. J.*, 2020, **26**, 8774–8783.
21 S. Benmansour and C. J. Gómez-García, *Magnetochemistry*, 2020, **6**, 1–44.
22 N. Monni, M. Sanna Angotzi, M. Oggianu, S. Ashoka Sahadevan and M. L. Mercuri, *J. Mater. Chem. C*, 2022, **10**, 1548–1572.
23 N. Monni, M. Oggianu, S. A. Sahadevan and M. L. Mercuri, *Magnetochemistry*, 2021, **7**, 1–12.
24 J. Flores Gonzalez, V. Montigaud, V. Dorcet, K. Bernot, B. Le Guennic, F. Pointillart and O. Cador, *Chem.–Eur. J.*, 2021, **27**, 10160–10168.
25 F. Pointillart, J. Flores Gonzalez, V. Montigaud, L. Tesi, V. Cherkasov, B. Le Guennic, O. Cador, L. Ouahab, R. Sessoli and V. Kuropatov, *Inorg. Chem. Front.*, 2020, **7**, 2322–2334.
26 W. Gauβ, H. Heitzer and S. Petersen, *Justus Liebigs Ann. Chem.*, 1973, **764**, 131–144.
27 C. J. Kingsbury, B. F. Abrahams and R. Robson, *CCDC 1568063: Experimental Crystal Structure Determination*, 2017.
28 N. Monni, E. Andres-Garcia, K. Caamaño, V. García-López, J. M. Clemente Juan, M. Giménez-Marqués, M. Oggianu, E. Cadoni, G. Mínguez Espallargas, M. Clemente Leon, M. L. Mercuri and E. Coronado, *J. Mater. Chem. A*, 2021, **9**, 25189–25195.
29 M. Llunell, D. Casanova, J. Cirera, P. Alemany and S. Alvarez, *SHAPE, version 2.1*, University of Barcelona, Spain, 2013.
30 M. P. Van Koeverden, B. F. Abrahams, D. M. D'Alessandro, P. W. Doheny, C. Hua, T. A. Hudson, G. N. L. Jameson, K. S. Murray, W. Phonsri, R. Robson and A. L. Sutton, *Chem. Mater.*, 2020, **32**, 7551–7563.
31 S. Benmansour, I. Pérez-Herráez, C. Cerezo-Navarrete, G. López-Martínez, C. Martínez Hernández and C. J. Gómez-García, *Dalton Trans.*, 2018, **47**, 6729–6741.
32 J. J. Baldoví, S. Cardona-Serra, J. M. Clemente-Juan, E. Coronado, A. Gaita-Ariño and A. Palii, *J. Comput. Chem.*, 2013, **34**, 1961–1967.
33 J. J. Baldoví, J. J. Borrás-Almenar, J. M. Clemente-Juan, E. Coronado and A. Gaita-Ariño, *Dalton Trans.*, 2012, **41**, 13705–13710.
34 K. Hymas and A. Soncini, *Phys. Rev. B*, 2021, **104**, 205306.
35 L. Escalera-Moreno, J. J. Baldoví, A. Gaita-Ariño and E. Coronado, *Chem. Sci.*, 2018, **9**, 3265–3275.
36 N. Monni, J. J. Baldoví, V. García-López, M. Oggianu, E. Cadoni, M. L. Mercuri, M. Clemente-León and E. Coronado, 2022, Manuscript in Preparation.
37 W. R. Reed, M. A. Dunstan, R. W. Gable, W. Phonsri, K. S. Murray, R. A. Mole and C. Boskovic, *Dalton Trans.*, 2019, **48**, 15635–15645.
38 P. Zhang, M. Perfetti, M. Kern, P. P. Hallmen, L. Ungur, S. Lenz, M. R. Ringenberg, W. Frey, H. Stoll, G. Rauhut and J. Van Slageren, *Chem. Sci.*, 2018, **9**, 1221–1230.
39 R. Ishikawa, S. Michiwaki, T. Noda, K. Katoh, M. Yamashita and S. Kawata, *Magnetochemistry*, 2019, **5**, 30.
40 F. Quochi, M. Saba, F. Artizzu, M. L. Mercuri, P. Deplano, A. Mura and G. Bongiovanni, *J. Phys. Chem. Lett.*, 2010, **1**, 2733–2737.
41 R. Marin, G. Brunet and M. Murugesu, *Angew. Chem., Int. Ed.*, 2021, **60**, 1728–1746.
42 F. Artizzu, L. Marchiò, M. L. Mercuri, L. Pilia, A. Serpe, F. Quochi, R. Orrù, F. Cordella, M. Saba, A. Mura, G. Bongiovanni and P. Deplano, *Adv. Funct. Mater.*, 2007, **17**, 2365–2376.